

TRACING THE EQUILIBRIUM PATHS OF COMPLEX ELASTIC RETICULATED SYSTEMS BY MEANS OF THE 'ADMISSIBLE DIRECTIONS CONE' METHOD

Salvatore Ligarò and Paolo Valvo

Department of Structural Engineering
Università degli Studi di Pisa, Italy
e-mail: s.ligarò@ing.unipi.it, p.valvo@ing.unipi.it

Keywords: Space truss, path tracing, arc-length method, bifurcation, turning point

Abstract. *Standard arc-length methods, which use a constant step-length, may encounter serious difficulties when tracing the equilibrium paths of 'perfect' or 'quasi-perfect' structural systems. In these cases, in the neighbourhood of bifurcation or sharp turning points, erroneous jumps of the algorithm onto different branches are always possible.*

These drawbacks can be efficiently overcome by using a self-adapting strategy able to reduce the assigned step-length according to the complexity of the curve. In particular, based on the concept of osculating circle, an inequality constraint is introduced, which forces the secant vector to fall within a prescribed 'cone of admissible directions' at each incremental step. The main advantage of this strategy is that it naturally leads to a uniformly accurate sampling of points along the path.

The method's effectiveness is moreover illustrated through its application to the stability analysis of complex reticulated systems, such as Schwedler domes and three-dimensional masts. In particular, the influence of different bracing patterns on their post-critical behaviour is examined.

1. Introduction

A natural consequence of the economical employment of new high-strength, high-performance materials is that contemporary structures are ever lighter and slenderer. Thus, dead loads now play a much less important role than in older structures, and their stabilising effects are either vanishing or wholly lacking. Consequently, today structures are for the most part subjected to service and accidental loads whose distributions and magnitudes are only partly predictable. In such circumstances, well-pondered judgements about structural strength and stability cannot be advanced without recourse to accurate large displacement analysis.

Within an FEM framework, this requires solving the set of non-linear equilibrium equations for the n unknown nodal displacements, u_1, u_2, \dots, u_n , of the discrete model subjected to prescribed loads. In the simplest case, these vary in magnitude by a single scalar multiplier, λ , so that solutions can be related to the point set of one or more curves of the $n+1$ -dimensional space with co-ordinates $\lambda, u_1, u_2, \dots, u_n$, which constitute the *equilibrium path*. The point ($\lambda=0$; $\mathbf{u}=\mathbf{0}$) belongs to the path and represents the reference solution. Moreover, the curve passing through it is, by convention, called the *primary branch*, while other curves, if any, are said to be *secondary branches*.

Incremental-iterative procedures represent the path as a broken line of chords, whose endpoints correspond to consecutive values of the representation parameter, η . Amongst these procedures, arc-length methods ([1], [2]) are unique in that they use an approximation of the curvilinear abscissa, s , as the parameter, thus path tracing can continue beyond limit points.

If the main goal of the analysis is to determine the first failure mode (generally local in nature), then path tracing may well be limited to a short initial arc corresponding to the beginning stage of the loading process until the first critical point (limit or bifurcation) is encountered. On the other hand, if one is instead interested in finding the structure's ultimate bearing capacity and, possibly, obtaining a better understanding of the sequence of all the local failure modes which precede final collapse, then tracing the entire path becomes necessary. In this case, one should remember that, according to the degree of imperfection of the structural system (geometry and load), equilibrium paths exhibit a wide gamut of post-critical behaviour, including simple and multiple bifurcation, snapping, multi-loops, sharp turning points and, probably, some other as yet unknown 'strange' phenomena.

In the first case, analysis can be carried out until an optimal *constant* parameter increment $\overline{\Delta\eta}$ is determined, which economically furnishes an accurate estimate of the sought critical point. In the second circumstance, however, adopting a constant step-length may be inappropriate or even misleading. In fact, small step-lengths unavoidably lead to inefficient and demanding computation, whilst large values may cause the algorithm to fail along arcs of greater curvature or in the neighbourhood of a bifurcation. In these cases, failure of the algorithm, due to undesired jumps, is revealed by sudden direction changes of the tangent to the path.

In [4] we proposed a self-adapting strategy, which uses the concept of osculating circle to step-wise find an optimal parameter increment. In particular, an upper limit to the change in angle experienced by the tangent vector at each incremental step is indirectly imposed by constraining the secant vector to fall within a prescribed *cone of admissible directions*. At any

given step, this cone is placed with its vertex at the last detected point, its axis coinciding with the tangent to the path, while its half-cone angle is kept constant along the entire path. The cone is defined by an inequality constraint added to the usual set of $n+1$ non-linear resolving equations. When this constraint operates together with the equality constraint defining the representation parameter increment (*auxiliary equation*), it permits unambiguous detection of the successive point, by performing, where necessary, automatic reduction of the step-length according to the local path curvature.

In this paper, the essentials of the algorithm are given in some detail, although the main attention is focused on its application in deducing the non-linear response of complex reticulated systems. In particular, cases of Schwedler domes and three-dimensional masts with different bracing patterns will be presented. An unexpected result of this study is that the arrangement of secondary diagonal bars, which does not affect the linear response, instead proves crucial in defining the non-linear behaviour of such structures.

2. Large displacement analysis of elastic reticulated systems

The following analysis concerns elastic reticulated systems of general shape under conservative loading. The mechanical model admits large nodal displacements, while deformation in the bars remain small or moderate. Moreover, a Total Lagrangian formulation is used throughout.

A system is composed by N joints connected to each other by M bars according to an assigned connectivity matrix, \mathbf{B} . Joints behave as ideal hinges, while bars are rectilinear and made of a linear elastic material. Loads, whose magnitudes vary proportionally with the single parameter $\lambda \in \mathbf{R}$, act exclusively upon the joints. Finally, the geometry is described with reference to a fixed rectangular co-ordinate system O, x, y, z .

Let C_0 be the configuration of the structure in a stress-free state ($\lambda=0$) assumed as a reference.

In it, the joints occupy positions $\mathbf{X}_I = [X_I, Y_I, Z_I]^T$, $I = 1, 2, \dots, N$, while the bar which connects joints I and J has length L_{IJ} and cross-sectional area A_{IJ} .

When the structure is subjected to the loads

$$\mathbf{P}_I = \lambda \mathbf{p}_I, \quad I = 1, 2, \dots, N, \quad (1)$$

where each $\mathbf{p}_I = [p_{xI}, p_{yI}, p_{zI}]^T$ is a nodal reference vector, the configuration changes from C_0 to C . Thus, joints undergo the nodal displacements \mathbf{u}_I , $I = 1, 2, \dots, N$, and assume the new positions $\mathbf{x}_I = \mathbf{X}_I + \mathbf{u}_I$.

As loads do not depend upon C , the load potential energy of the system is defined as

$$V = V(\lambda; \mathbf{u}) = \sum_{I=1}^N V_I = \sum_{I=1}^N (-\lambda \mathbf{p}_I \cdot \mathbf{u}_I) = -\lambda \mathbf{p} \cdot \mathbf{u}, \quad (2)$$

where vectors $\mathbf{p}, \mathbf{u} \in \mathbf{R}^n$, $n = 3N$, collect nodal loads and displacements.

By our initial assumptions, the Green-Lagrange tensor and conjugate second Piola-Kirchhoff tensor are adopted as measures of strain and stress, respectively. The strain energy for bar IJ can be expressed in the form

$$W_{IJ} = \frac{1}{2} \begin{bmatrix} \mathbf{u}_I \\ \mathbf{u}_J \end{bmatrix} \cdot \begin{bmatrix} \mathbf{D}_{IJ} & -\mathbf{D}_{IJ} \\ -\mathbf{D}_{IJ} & \mathbf{D}_{IJ} \end{bmatrix} \begin{bmatrix} \mathbf{u}_I \\ \mathbf{u}_J \end{bmatrix}, \quad (3)$$

where

$$\mathbf{d}_{IJ} = \mathbf{X}_J + 1/2\mathbf{u}_J - (\mathbf{X}_I + 1/2\mathbf{u}_I) \quad (4)$$

is the intermediate bar position vector, $\mathbf{D}_{IJ} = H_{IJ}[\mathbf{d}_{IJ} \otimes \mathbf{d}_{IJ}]$ is a 3×3 sub-matrix, and the constant $H_{IJ} = E_{IJ}A_{IJ}/L_{IJ}^3$ groups bar properties.

By summing contributions (3), the strain energy of the system results to be

$$W(\mathbf{u}) = \frac{1}{2} \mathbf{u} \cdot \mathbf{D}(\mathbf{u})\mathbf{u}, \quad (5)$$

where the matrix $\mathbf{D}(\mathbf{u}) \in \mathbb{R}^{n \times n}$ stems from assembling the sub-matrices \mathbf{D}_{IJ} .

Finally, by summing (2) and (5), we obtain the system's total potential energy,

$$\Pi(\lambda; \mathbf{u}) = W(\mathbf{u}) + V(\lambda; \mathbf{u}) = \frac{1}{2} \mathbf{u} \cdot \mathbf{D}(\mathbf{u})\mathbf{u} - \lambda \mathbf{p} \cdot \mathbf{u}, \quad (6)$$

as a function of λ and \mathbf{u} . For assigned λ , if the system is to be in equilibrium in C, it is necessary that $\Pi(\lambda; \mathbf{u})$ be stationary with respect to each component of \mathbf{u} . Consequently,

$$\frac{\partial \Pi(\lambda; \mathbf{u})}{\partial \mathbf{u}} = \mathbf{f}(\lambda; \mathbf{u}) = \mathbf{0}, \quad (7)$$

which form a set of n non-linear equations for the unknowns u_1, u_2, \dots, u_n . In (7), $\mathbf{f}(\lambda; \mathbf{u})$ is a vector collecting nodal resultant forces. From (7), the balance equations for the generic bar IJ can be extracted as

$$\begin{bmatrix} \mathbf{f}_I \\ \mathbf{f}_J \end{bmatrix} = \begin{bmatrix} \mathbf{K}_{IJ} & -\mathbf{K}_{IJ} \\ -\mathbf{K}_{IJ} & \mathbf{K}_{IJ} \end{bmatrix} \begin{bmatrix} \mathbf{u}_I \\ \mathbf{u}_J \end{bmatrix} - \lambda \begin{bmatrix} \mathbf{p}_I \\ \mathbf{p}_J \end{bmatrix} = \begin{bmatrix} \mathbf{0} \\ \mathbf{0} \end{bmatrix}, \quad (8)$$

where

$$\mathbf{K}_{IJ} = \mathbf{D}_{IJ} + \frac{1}{2} H_{IJ} (\mathbf{u}_J - \mathbf{u}_I) \otimes \mathbf{d}_{IJ}. \quad (9)$$

This permits system (7) to be written out as

$$\mathbf{f}(\lambda; \mathbf{u}) = \mathbf{K}(\mathbf{u})\mathbf{u} - \lambda\mathbf{p} = \mathbf{0}, \quad (10)$$

where $\mathbf{K}(\mathbf{u}) \in \mathbf{R}^{n \times n}$ is the secant stiffness matrix of the structure.

Solutions to system (10), corresponding to a continuously variable λ , furnish the *equilibrium path* of the structure in the $\lambda, u_1, u_2, \dots, u_n$ co-ordinate space.

3. Path tracing via standard arc-length methods

Whatever representation parameter η is chosen, it is usually entered by an *auxiliary equation* of the form

$$f_0(\lambda; \mathbf{u}; \eta) = 0, \quad (11)$$

to be added to the equilibrium equations (10), yielding the *augmented system*

$$\begin{cases} f_0(\lambda; u_h; \eta) = 0 \\ f_i(\lambda; u_h) = K_{ij}(u_h)u_j - \lambda p_i = 0, \quad i, j, h = 1, 2, \dots, n. \end{cases} \quad (12)$$

Through the following change of variables

$$\begin{cases} t_0 = \mu_0 \lambda \\ t_i = u_i, \quad i = 1, 2, \dots, n, \end{cases} \quad (13)$$

where $\mu_0 \in \mathbf{R}^+$ is a scaling factor, the load parameter, λ , and the nodal displacements, u_1, u_2, \dots, u_n , are placed on an equal basis. Thus, tracing the path entails solving the system

$$f_\alpha(t_\beta; \eta) = 0, \quad \alpha, \beta = 0, 1, 2, \dots, n \quad (14)$$

for increasing discrete values $\eta^{(1)}, \eta^{(2)}, \dots, \eta^{(K)}$ of the chosen parameter.

At any given step K , corresponding to $\eta^{(K)}$, the point location $\mathbf{t}^{(K)}$ and the unit tangent vector to the path $\dot{\mathbf{t}}^{(K)}$ (where the dot denotes differentiation with respect to the curvilinear abscissa, s) are both known. So, the problem consists of finding the next point $\mathbf{t}^{(K+1)}$ or, alternatively, the *secant vector*, $\Delta \mathbf{t}^{(K)} = \mathbf{t}^{(K+1)} - \mathbf{t}^{(K)}$, relative to the value $\eta^{(K+1)} = \eta^{(K)} + \overline{\Delta \eta}$, where $\overline{\Delta \eta}$ is the assigned increment.

Of the various available forms for equation (11), we adopt the definition by Crisfield [3]

$$f_0(\mathbf{t}; \overline{\Delta\eta}) = [\mathbf{t}^{(K+1)} - \mathbf{t}^{(K)}]^2 - \overline{\Delta\eta}^2 = [\Delta\mathbf{t}^{(K)}]^2 - \overline{\Delta\eta}^2 = 0, \quad (15)$$

which imposes that the next point $\mathbf{t}^{(K+1)}$ belong to the sphere of radius $\overline{\Delta\eta}$, with centre at $\mathbf{t}^{(K)}$. Thus, the parameter increment coincides with the length of the secant vector $\overline{\Delta\eta} = \|\Delta\mathbf{t}^{(K)}\| \cong \overline{\Delta s}$.

A predictor-corrector scheme is then applied to system (14) to find $\Delta\mathbf{t}^{(K)}$. In particular, the first estimate is given by the linear predictor

$$\Delta\mathbf{t}^{(K,0)} = \overline{\Delta\eta} \dot{\mathbf{t}}^{(K)}, \quad (16)$$

while improved estimates $\Delta\mathbf{t}^{(K,1)}$, $\Delta\mathbf{t}^{(K,2)}$, ..., $\Delta\mathbf{t}^{(K,H)}$ are obtained by consecutive iterations. At cycle H , the Newton-Raphson method furnishes the updated secant vector

$$\begin{cases} \Delta\mathbf{t}_*^{(K,H+1)} = \Delta\mathbf{t}^{(K,H)} - \left[\begin{array}{c} 2\Delta\mathbf{t}^{(K,H)\text{T}} \\ -\mathbf{p} \quad \mathbf{K}_T(\mathbf{u}^{(K+1,H)}) \end{array} \right]^{-1} \mathbf{f}(\mathbf{t}^{(K+1,H)}; \eta) \\ \Delta\mathbf{t}^{(K,H+1)} = \mathbf{t}^{(K,H+1)} - \mathbf{t}^{(K)} = \overline{\Delta\eta} \frac{\Delta\mathbf{t}_*^{(K,H+1)}}{\|\Delta\mathbf{t}_*^{(K,H+1)}\|} \end{cases} \quad (17)$$

where $\mathbf{K}_T(\mathbf{u}) = \partial\mathbf{f}(\lambda; \mathbf{u})/\partial\mathbf{u} \in \mathbf{R}^{n \times n}$ is the tangent stiffness matrix of the structure and the obtained secant vector, $\Delta\mathbf{t}_*^{(K,H+1)}$, is further scaled to fit the spherical constraint (15).

Iterations are continued until $\|\Delta\mathbf{t}^{(K,H+1)} - \Delta\mathbf{t}^{(K,H)}\|/\sqrt{\overline{\Delta\eta}}$ is smaller than a given dimensionless tolerance, TOL . At convergence, the unit tangent vector, $\dot{\mathbf{t}}^{(K+1)}$, is found from the system

$$\begin{cases} \left[\begin{array}{c} (\dot{\mathbf{t}}^{(K)})^T \\ -\mathbf{p} \quad \mathbf{K}_T(\mathbf{u}^{(K+1)}) \end{array} \right] \dot{\mathbf{t}}_*^{(K+1)} = \mathbf{e}_0 \\ \dot{\mathbf{t}}^{(K+1)} = \frac{\dot{\mathbf{t}}_*^{(K+1)}}{\|\dot{\mathbf{t}}_*^{(K+1)}\|} \end{cases} \quad (18)$$

where \mathbf{e}_0 is the first unit vector of the canonical basis of \mathbf{R}^{n+1} , and the obtained tangent vector, $\dot{\mathbf{t}}_*^{(K+1)}$, is further scaled to the unit norm.

4. The cone of admissible directions

Large displacement analysis of real structural systems inevitably leads to trace equilibrium paths, which at first sight may appear very tangled and endowed with seemingly inextricable knots. Some typical examples will be presented in what follows. Their tracing was made possible by virtue of a self-adapting strategy able to correct the parameter increment according to the complexity of the curve. The basic idea of the strategy consists of setting an upper limit to the change in angle experienced by the unit tangent vector within each incremental step. The concept of osculating circle is used to this end, so the resulting algorithm integrates well with standard arc-length methods.

4.1. Basic idea and definition

Figure 1(a) shows two points, $\mathbf{t}^{(K)}$ and $\mathbf{t}^{(K+1)}$, on the equilibrium path relative to two consecutive incremental steps, as well as the corresponding unit tangent vectors, $\dot{\mathbf{t}}^{(K)}$ and $\dot{\mathbf{t}}^{(K+1)}$, the unit principal normal vector $\mathbf{n}^{(K)}$ and the osculating circle $\Gamma^{(K)}$ at $\mathbf{t}^{(K)}$, whose radius is $\rho^{(K)}$. If points $\mathbf{t}^{(K)}$ and $\mathbf{t}^{(K+1)}$ are sufficiently near each other, the path segment connecting them is indistinguishable from a small arc of $\Gamma^{(K)}$.

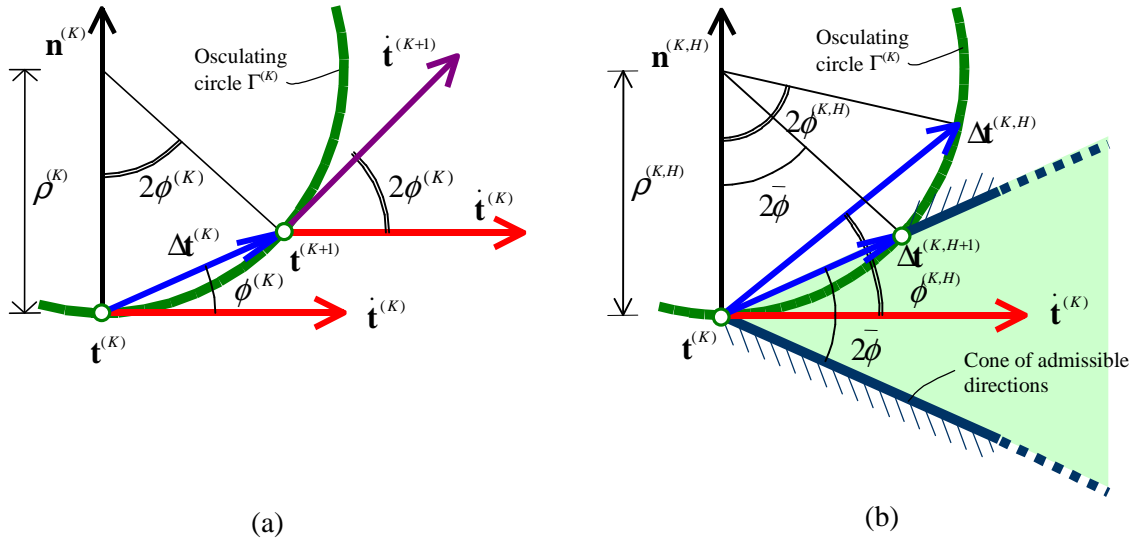


Figure 1: The cone of admissible directions

A simple geometric argument demonstrates that the angle formed by $\dot{\mathbf{t}}^{(K)}$ and $\dot{\mathbf{t}}^{(K+1)}$ is twice the angle, $\phi^{(K)}$, between $\dot{\mathbf{t}}^{(K)}$ and $\Delta\mathbf{t}^{(K)}$. Hence, limiting the angle change experienced by $\dot{\mathbf{t}}$ during the incremental step K is equivalent to imposing the following inequality constraint

$$\phi^{(K)} \leq \bar{\phi}, \quad (19)$$

which defines the *cone of admissible directions*, within which the secant vector, $\Delta \mathbf{t}^{(K)}$, must fall. This cone has vertex at $\mathbf{t}^{(K)}$, axis $\dot{\mathbf{t}}^{(K)}$ and constant half-cone angle $\bar{\phi}$ (Figure 1(b)).

4.2. Implementation

At the end of iterative cycle H , the angle between the currently evaluated secant vector, $\Delta \mathbf{t}^{(K,H)}$, and the known unit tangent vector, $\dot{\mathbf{t}}^{(K)}$, is given by

$$\cos \phi^{(K,H)} = \frac{\Delta \mathbf{t}^{(K,H)} \cdot \dot{\mathbf{t}}^{(K)}}{\|\Delta \mathbf{t}^{(K,H)}\|}. \quad (20)$$

When $\phi^{(K,H)} > \bar{\phi}$, the current step-length $\Delta \eta^{(K,H)}$ is reduced to

$$\Delta \eta^{(K,H+1)} = \frac{\sin \bar{\phi}}{\sin \phi^{(K,H)}} \|\Delta \mathbf{t}^{(K,H)}\|, \quad (21)$$

and the new corrector

$$\Delta \mathbf{t}^{(K,H+1)} = \Delta \eta^{(K,H+1)} \left(\sin \bar{\phi} \mathbf{n}^{(K,H)} + \cos \bar{\phi} \dot{\mathbf{t}}^{(K)} \right) \quad (22)$$

is obtained, where $\mathbf{n}^{(K,H)}$ is the unit principal normal vector at $\mathbf{t}^{(K)}$ evaluated at cycle H . Equation (22) defines the secant vector as that joining point $\mathbf{t}^{(K)}$ to the point where the cone of admissible directions intersects the osculating circle.

By projecting $\Delta \mathbf{t}^{(K,H)}$ on the plane perpendicular to $\dot{\mathbf{t}}^{(K)}$, we obtain

$$\mathbf{n}^{(K,H)} = \frac{(\mathbf{I} - \dot{\mathbf{t}}^{(K)} \otimes \dot{\mathbf{t}}^{(K)}) \Delta \mathbf{t}^{(K,H)}}{\|(\mathbf{I} - \dot{\mathbf{t}}^{(K)} \otimes \dot{\mathbf{t}}^{(K)}) \Delta \mathbf{t}^{(K,H)}\|} = \frac{1}{\sin \phi} \frac{\Delta \mathbf{t}^{(K,H)}}{\|\Delta \mathbf{t}^{(K,H)}\|} - \cot \phi \dot{\mathbf{t}}^{(K)}, \quad (23)$$

where \mathbf{I} is the identity tensor. Finally, by combining equations (22) and (23), the expression for the corrector results to be

$$\Delta \mathbf{t}^{(K,H+1)} = \left(\frac{\sin \bar{\phi}}{\sin \phi^{(K,H)}} \right)^2 \Delta \mathbf{t}^{(K,H)} + \Delta \eta^{(K,H+1)} \frac{\sin(\phi^{(K,H)} - \bar{\phi})}{\sin \phi^{(K,H)}} \dot{\mathbf{t}}^{(K)}. \quad (24)$$

4.3. Computational aspects

In assigning specific values to the parameters $\overline{\Delta\eta}$ and $\overline{\phi}$, one must consider that they are not independent of each other. In fact, tracing accuracy can be assumed to be the reciprocal of $\delta = 1/2\overline{\Delta\eta} \tan\overline{\phi}$, which gives an estimate of the maximum distance from the broken line of chords to the equilibrium path. Consequently, in order to achieve the desired accuracy, either $\overline{\Delta\eta}$ or $\overline{\phi}$ can be assigned small values. However, when dealing with ‘perfect’ or ‘quasi-perfect’ reticulated systems, the limitation on the angle change must be made more severe, so that the algorithm will be effective in critical situations as well.

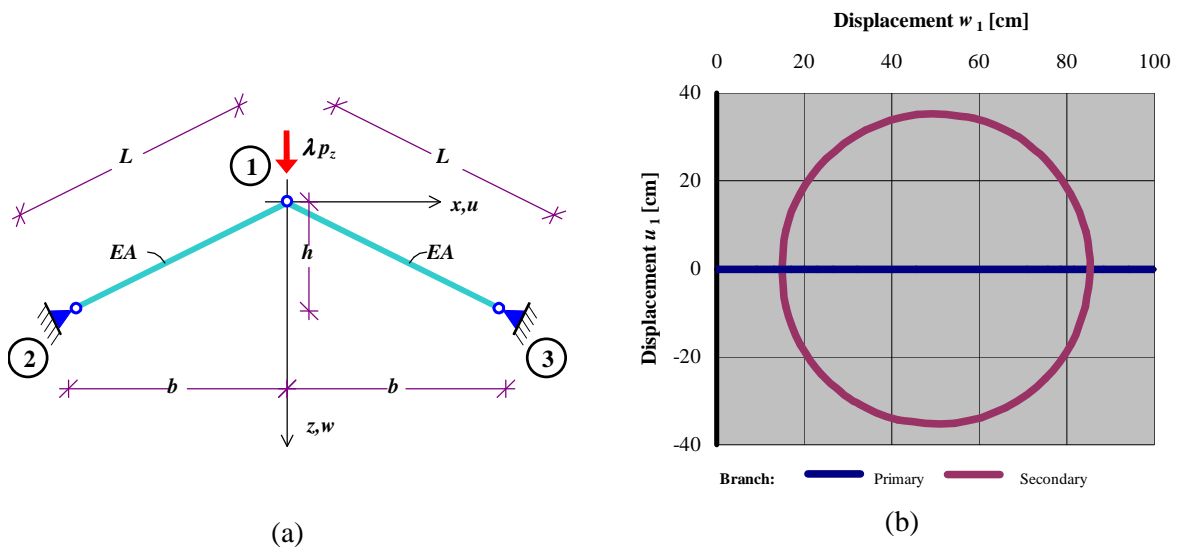


Figure 2: A perfect system and its path

In fact, in the case of a perfect system (Figure 2(a)), the equilibrium path consists of one or more smooth curves, the primary and secondary branches that intersect each other at bifurcation points (Figure 2(b)). Difficulties in path tracing stem mainly from secondary branches, whose number and location are unknown *a priori*. Thus, it is always possible for the algorithm to jump onto a different branch in the neighbourhood of an unexpected bifurcation. In order to avoid such an eventuality, small values of $\overline{\phi}$ are recommended because the constraint on $\overline{\Delta\eta}$ turns out to be ineffective for this purpose.

Likewise, when dealing with a quasi-perfect system (Figure 3(a)), we should consider it to be derived from a perfect one, in which the geometry or mechanical properties or, lastly, applied loads have been changed by some small but non-negligible imperfections capable of breaking the system’s symmetry in a barely perceptible way. Therefore, its equilibrium path (Figure 3(b)) is composed of one or more curves winding through space, keeping as close as possible to the path of the perfect system it derives from. In this case as well, small values of $\overline{\phi}$ are to be used, since the constraint on $\overline{\Delta\eta}$ alone does not permit accurately describing the load-

deflection response in the neighbourhood of sharp turning points.

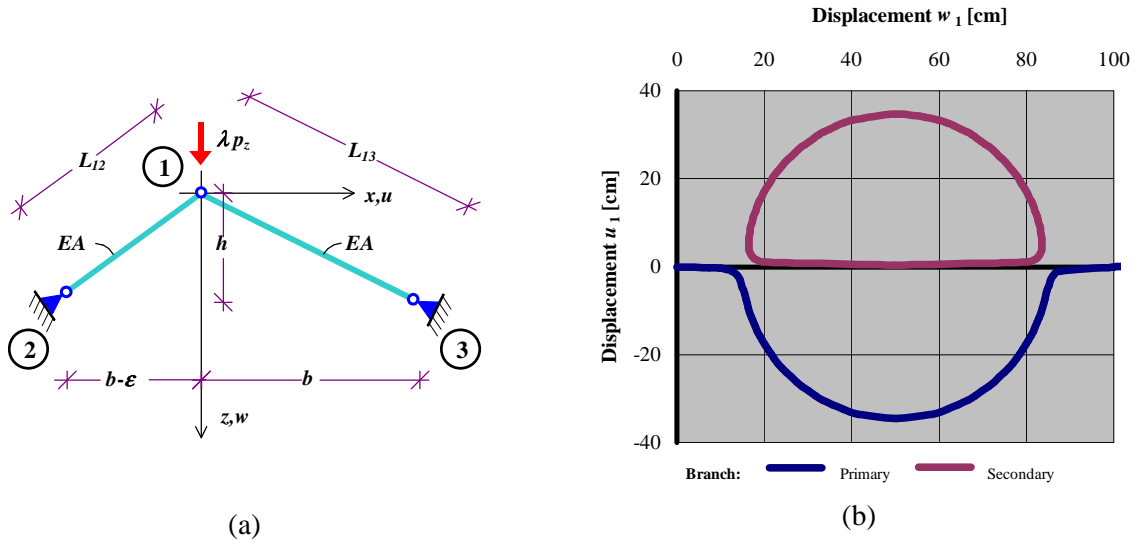


Figure 3: A quasi-perfect system and its path

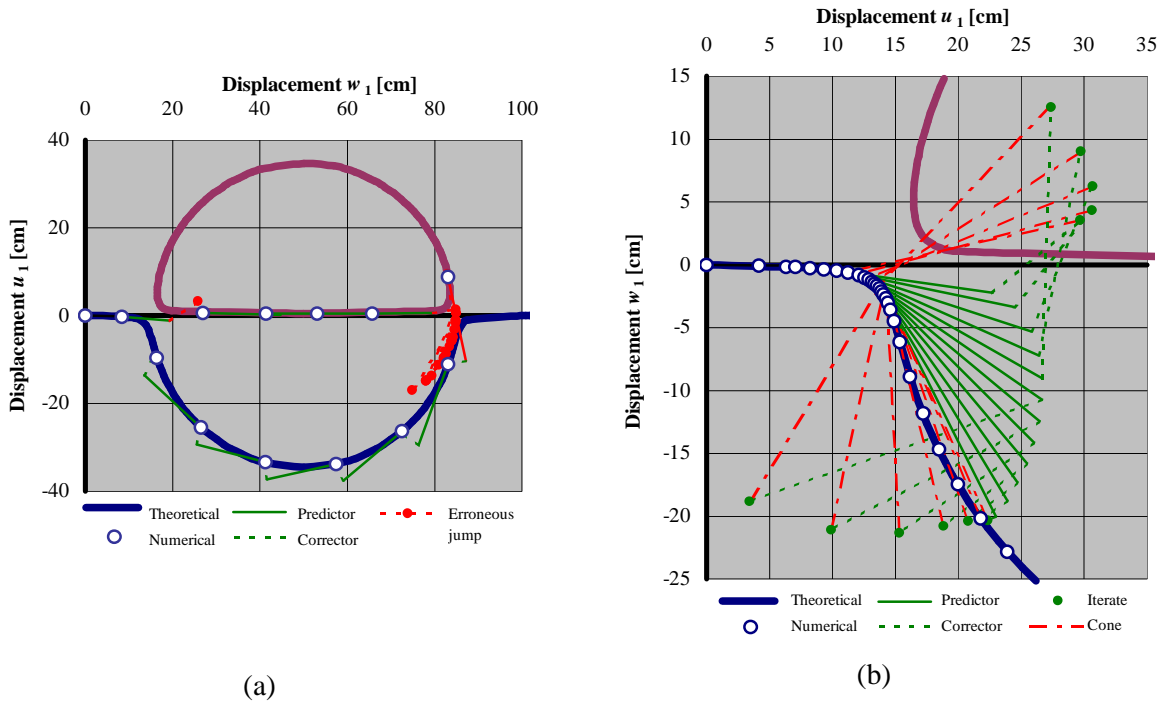


Figure 4: Tracing the path of a quasi-perfect system

For the sake of comparison, Figure 4 shows how a standard procedure and the proposed method behave in tracing the equilibrium path of the same quasi-perfect system containing sharp turning points. Figure 4(a) shows the results of the constant step-length procedure,

where an erroneous tracing occurs due to undesired jumps. Figure 4(b) instead presents a path detail in the neighbourhood of the turning point furnished by the proposed strategy, in which the finer sampling of points is evident.

Finally, the case of ‘imperfect’ reticulated systems (Figure 5(a)) proves to be the simplest to deal with, since turning points are usually smooth and no bifurcation is present (Figure 5(b)). Although the constraint on $\overline{\Delta\eta}$ alone generally works, a moderately small value of $\overline{\phi}$ can be used to achieve uniform accuracy in tracing.

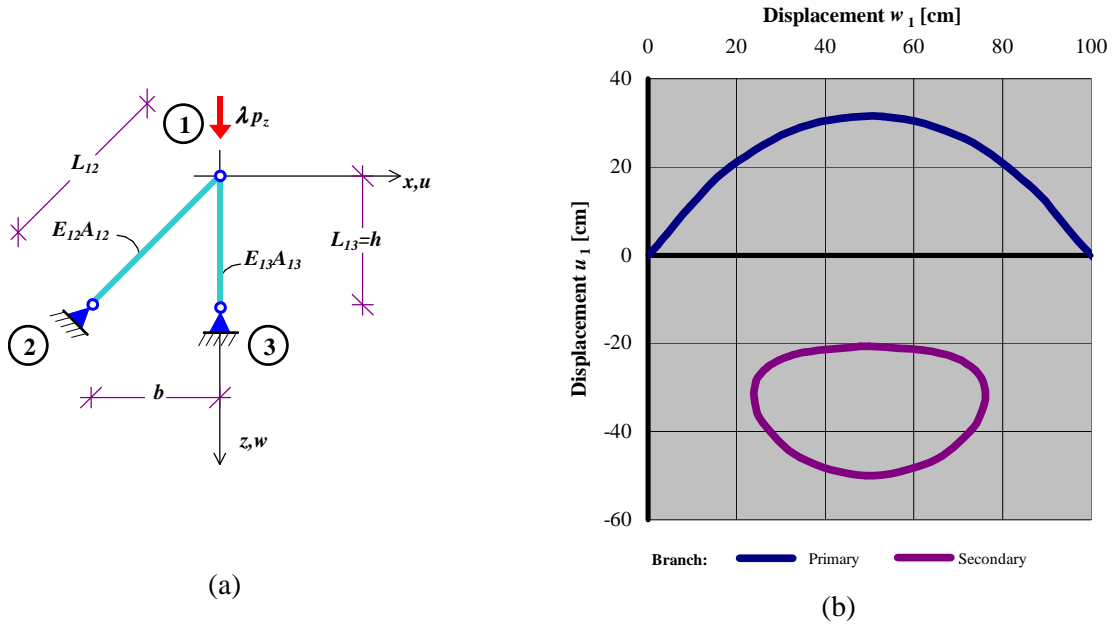


Figure 5: An imperfect system and its path

5. Applications

The described strategy is first applied herein to the stability analysis of a perfect 39 DOF Schwedler dome subjected to a vertical load on its upper joint. Two different bracing schemes are considered one after the other, and their effects on the primary branch are compared.

Next, the post-critical behaviour of a 75 DOF mast subjected simultaneously to vertical and horizontal loads on its upper joint is analysed. Once again, the effects of different bracing schemes are examined. This same structure, though subjected to a vertical load alone, has already been considered by Wriggers *et al.* [5] in testing a procedure for direct computation of stability points. Here, by gradually modifying the ratio of horizontal to vertical loads, we modify the character of the reticulated system from a perfect to an imperfect one, thus allowing a wide range of different responses to emerge.

5.1. A spirally braced Schwedler dome

A hemispherical Schwedler dome of radius 150 cm is depicted in Figure 6. The structure is made up of 19 joints (6 of which are fixed), connected to each other by 42 active bars of equal extensional stiffness, $EA = 2 \cdot 10^6 \text{ daN}$, though different in length. We presume that the cladding panels do not perform any static function.

A vertical load of magnitude $P_z = \lambda p_z = \lambda \cdot 5000 \text{ daN}$ acts upon the upper joint. Since the diagonal bars are arranged in a fashion resembling a spiral, the system possesses a six-fold rotational symmetry about the z -axis.

In keeping with the aforesaid considerations, a small value of the half-cone angle $\bar{\phi} = 0.05 \text{ rad}$ was used together with a step-length $\Delta\eta = 25 \text{ cm}$. The assumed scaling parameter was $\mu_0 = 1 \text{ cm}$ and the tolerance $TOL = 10^{-6}$.

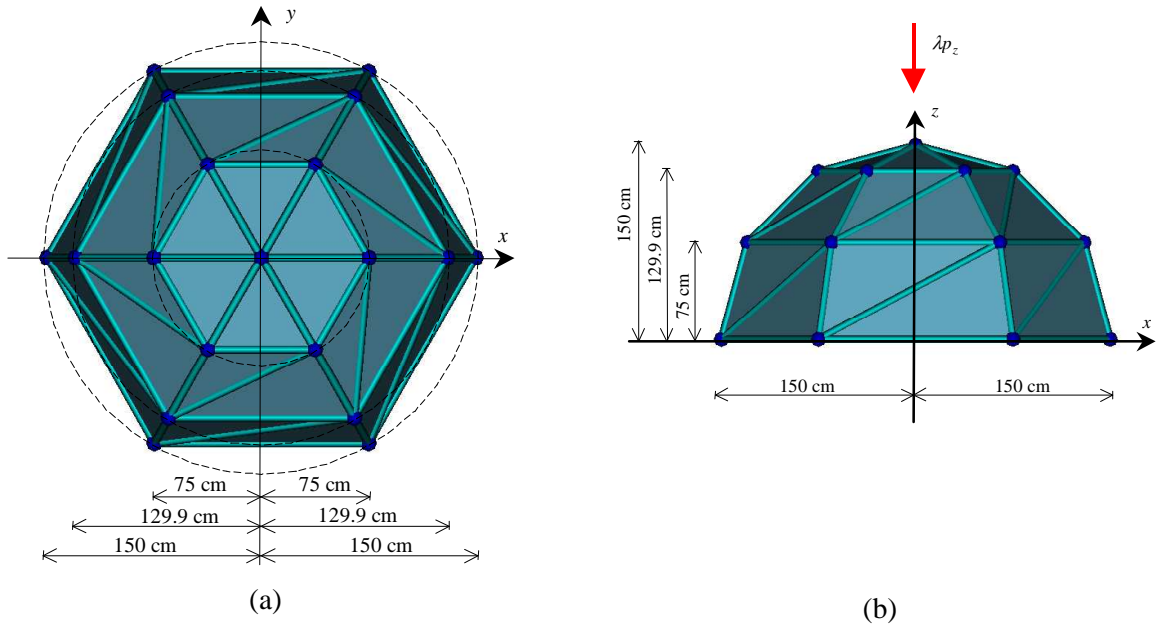


Figure 6: Spirally braced Schwedler dome – Geometry

Figure 7 shows the primary branch of the equilibrium path as furnished by the admissible directions cone method projected onto the plane O, λ, w_1 , where w_1 is the vertical displacement of the top joint. This branch would constitute the load-deflection response if both the load and displacements were simultaneously controlled. If, instead, the process occurs under load control alone, then the actual response reduces to its portion, OABCDEF, which appears in red in the figure. By examining the sequence of deformed configurations, it turns out that the continuous arcs correspond to stages of simultaneous ‘spinning’ and ‘lowering’ of the entire structure, while the dashed lines express dynamic snapping.

Structural behaviour is complicated only in appearance. In fact, if we idealise the dome as being made up of three superimposed layers joined to each other by two coaxial hexagons of

bars, then the structure can be viewed as a simple series system. The particular bracing arrangement forces each layer to rotate about the common z -axis, so the global structural response is that of a spinning top.

A noteworthy non-linearity in the load-deflection response appears right from the start of the loading process, OA. The upper joint snaps upon reaching the limit point A, $\lambda = 4.536$, when the structure's overall rotation is still moderate. After the second spinning phase, BC, the upper hexagon snaps at C, when $\lambda = 46.238$. Next, a stage of large spinning, DE, precedes the snapping of the lower hexagon at E, when $\lambda = 135.020$. Finally, at F the structure reaches a configuration that is nearly opposite the original one, O.

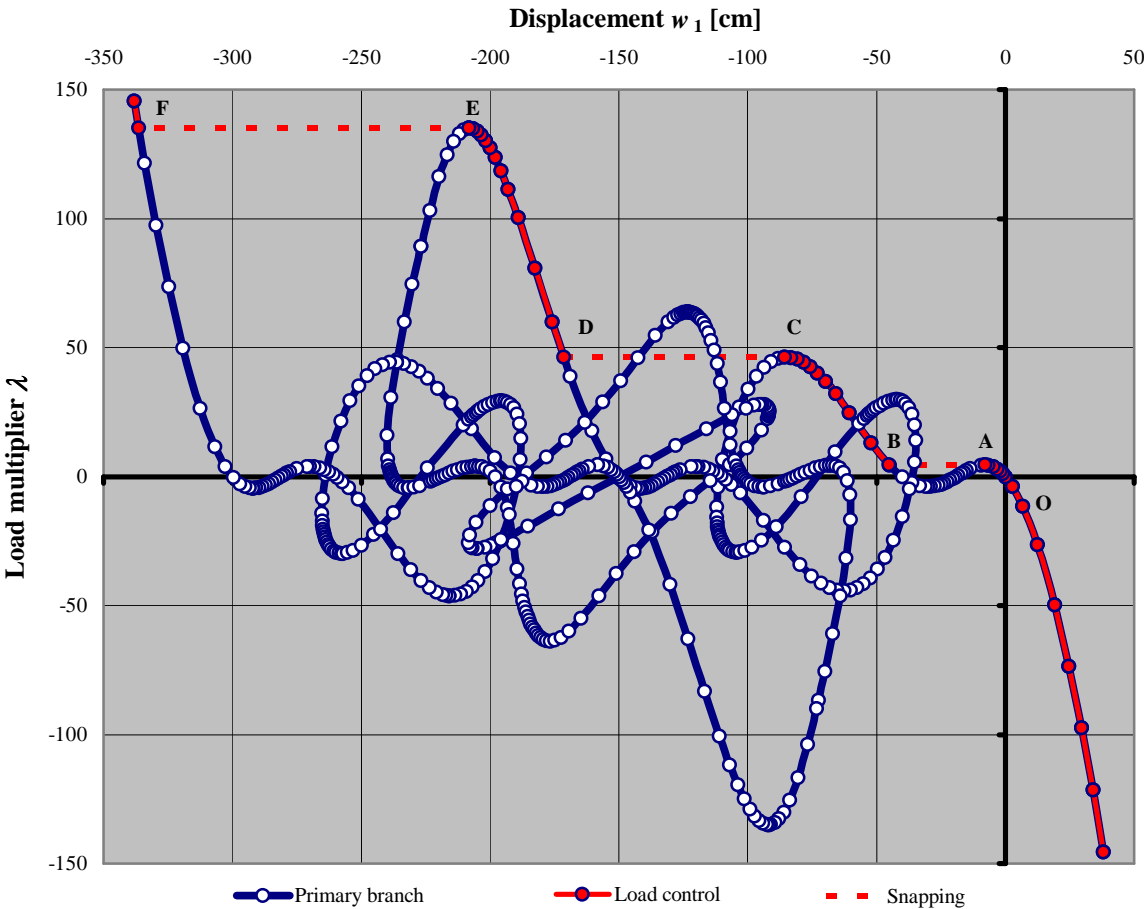


Figure 7: Spirally braced Schwedler dome – Primary branch – Joint 1

Figures 8(a) and 8(b) show the same primary branch, projected onto the planes O, λ, u_2 , and O, λ, v_2 , respectively, where u_2 and v_2 are the horizontal displacement components of a joint on the upper hexagon.

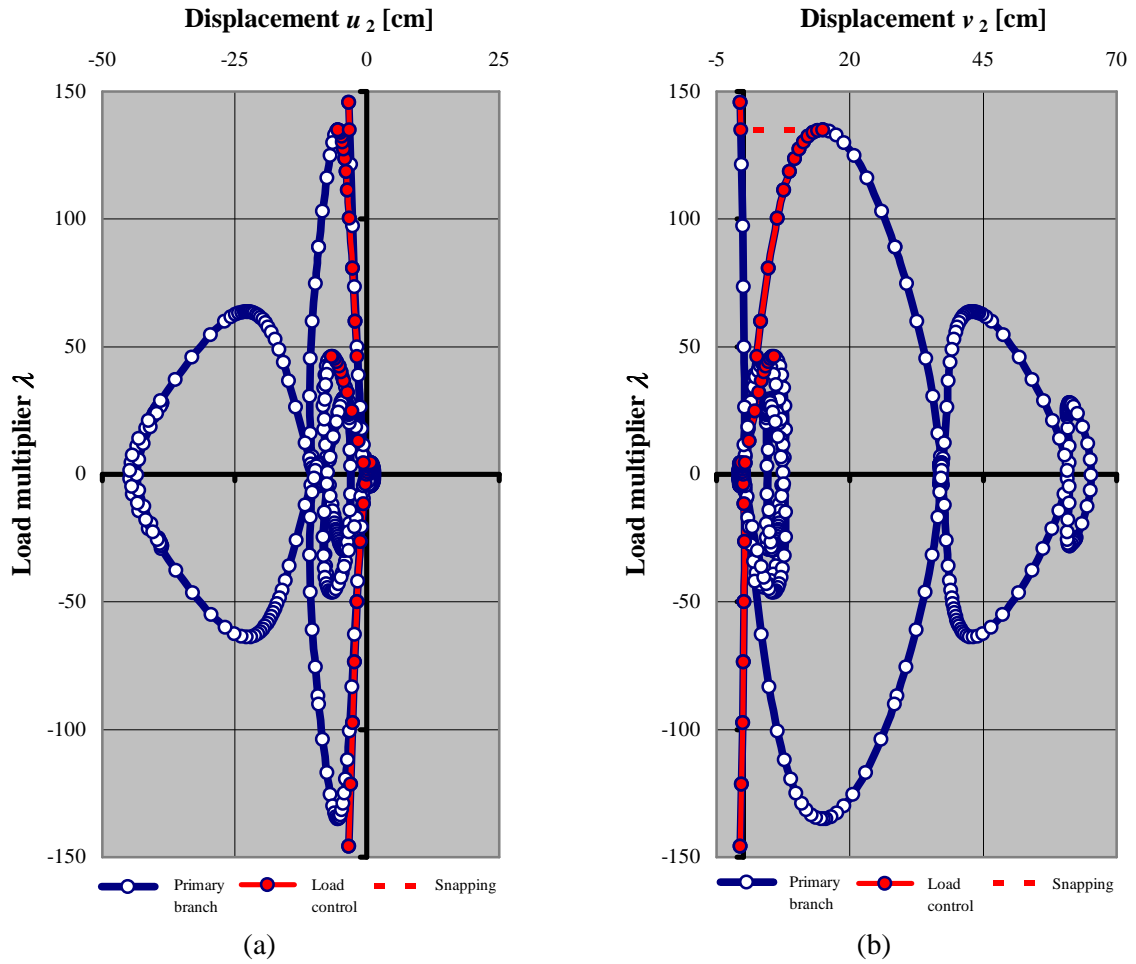


Figure 8: Spirally braced Schwedler dome – Primary branch – Joint 2

5.2. A symmetrically braced Schwedler dome

Figure 9 considers the previous hemispherical Schwedler dome with a different bracing pattern. Here, secondary diagonal bars are arranged in such a way as to oppose possible rotations about the z -axis. The system still possesses three-fold rotational symmetry. The values $\bar{\phi} = 0.05 \text{ rad}$ and $\bar{\Delta\eta} = 25 \text{ cm}$ were adopted, together with $\mu_0 = 1 \text{ cm}$ and $TOL = 10^{-6}$.

Figure 10 shows the primary branch of the equilibrium path projected onto the plane O, λ, w_1 . Actually, the path looks like a very complicated curve. Nevertheless, if one is interested in determining the structural behaviour under load control, then the actual response reduces once again to the simpler part, OABCDEF, which appears in red. Continuous arcs correspond to the stages of lowering alone where elastic energy is stored. This is later released in part during the dynamic snapping phases, represented by the dashed lines.

Contrary to linear analysis, comparison of Figures 7 and 10 clearly reveals how modification of the bracing scheme can cause strong variations in the non-linear response of the structure.

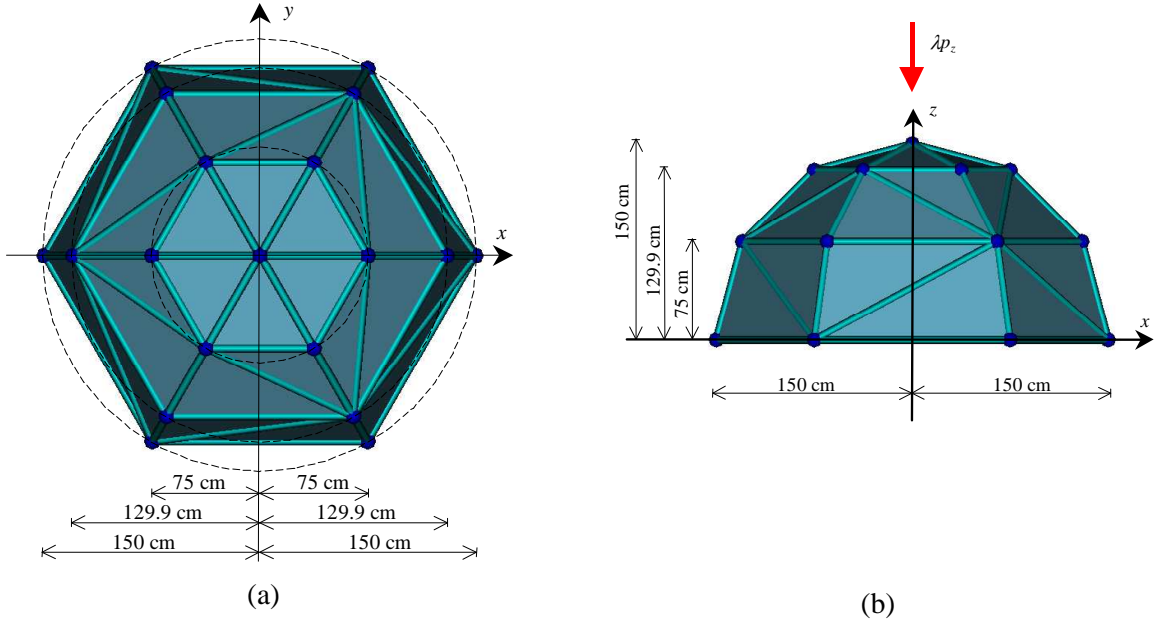


Figure 9: Symmetrically braced Schwedler dome – Geometry

The upper joint snaps upon reaching the limit point A. Since this local failure mode is insensitive to changes made in the bracing scheme, we found a load multiplier value, $\lambda = 4.569$, that is practically unchanged with respect to the previous case. After the second phase of energy storage, BC, the upper hexagon snaps at C, when $\lambda = 34.640$. In this case, due to the three-fold symmetry, the joints of the upper hexagon possess a different stiffness, so that they undergo out-of-plane displacements of alternating sign, and the hexagon warps before it snaps. Finally, a last storing phase, DE, precedes the snapping of the lower hexagon at E, when $\lambda = 267.425$. This value is nearly twice that found for the spirally braced case.

5.3. A spirally braced mast

Figure 12(O) shows the reference configuration of the three-dimensional mast previously considered by Wriggers *et al.* in [5]. Its gross dimensions are $7\text{ m} \times 7\text{ m}$ (basis) $\times 35\text{ m}$ (height). Further details can be found in the cited paper. Again, the structure is made up of 29 joints, 4 of which are fixed, connected one to the other by 79 bars of equal extensional stiffness, $EA = 6.3 \cdot 10^6\text{ daN}$, but different in length. Secondary bars are arranged to resemble a spiral, so that the structure possesses four-fold rotational symmetry about the z -axis.

In [5], a vertical load of magnitude $P_z = \lambda p_z = \lambda \cdot 5000\text{ daN}$ was considered to act upon the top joint, so the resulting reticulated system behaved as a perfect one. Non-linear buckling analysis was performed, and a multiple bifurcation point was detected for the load parameter $\lambda = 13.84$. Here, the system symmetry is instead broken by the addition of a disturbing horizontal load, $P_x = \lambda p_x$, so that the structural behaviour can be gradually converted from that of a quasi-perfect system to that of an imperfect one.

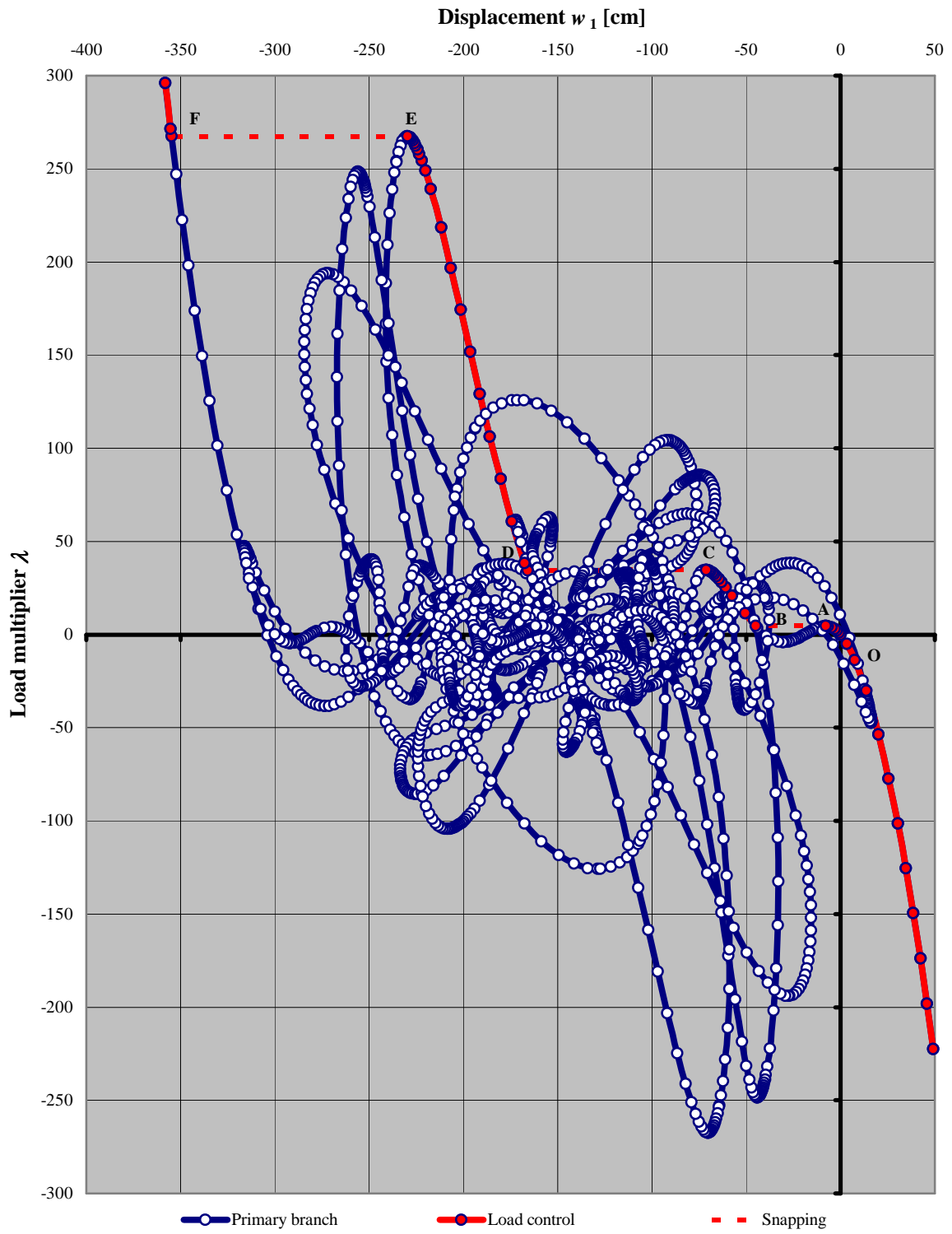


Figure 10: Symmetrically braced Schwedler dome – Equilibrium path – Joint 1

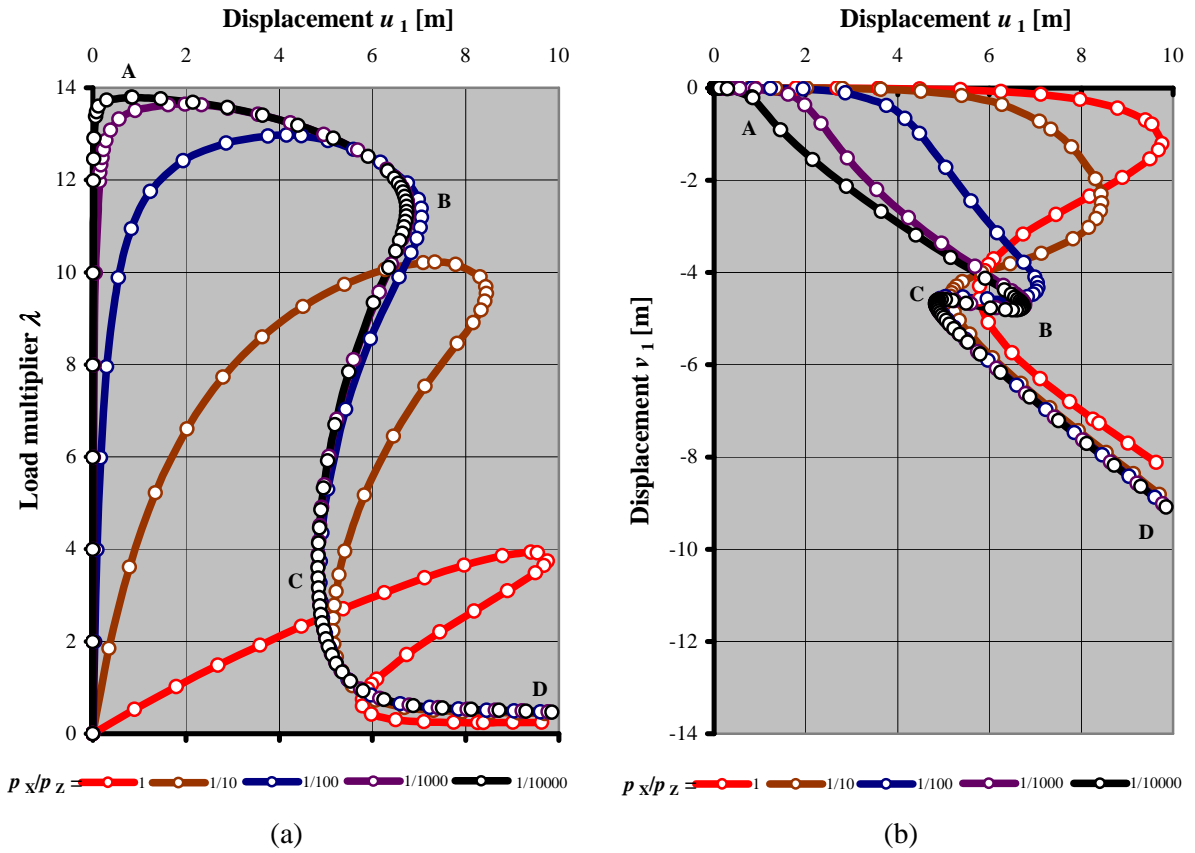


Figure 11: Spirally braced mast – Equilibrium path – Joint 1

Figures 11(a) and 11(b) show two different views of the primary branch relative to the load ratio values, p_x / p_z , presented in Table 1. The same table also reports the angle, $\bar{\phi}$, and the limit load multiplier, λ_{\max} . A step-length $\Delta\eta = 2 \text{ m}$ was used for the analyses, with $\mu_0 = 1 \text{ cm}$ and $TOL = 10^{-6}$.

p_x / p_z	1/1	1/10	1/100	1/1000	1/10000
$\bar{\phi}$	0.15	0.10	0.10	0.05	0.05
λ_{\max}	3.930	10.222	12.971	13.644	13.972

Table 1: Load ratio, half-cone angle and limit load multiplier for the spirally braced mast

A better understanding of structural behaviour can be achieved if we think of the mast as composed of seven superimposed substructures joined to each other by six groups of bars placed along the edges of coaxial squares. Additional bars stiffen three of these squares. With

this in mind, the structural behaviour reduces to that of a series system. If only a vertical load acts, the bracing arrangement forces each layer to rotate about the z -axis, and the global response is again characterised by a sequence of spinning phases. Overall lateral bending starts when the bifurcation is reached and develops following a secondary branch. Instead, in the presence of a disturbing horizontal load, the flexural behaviour appears right from the beginning of the loading process, and develops along the primary branch.

Figure 12 shows the sequence of equilibrium configurations for the load ratio $p_x / p_z = 1/10000$. During the initial phase OA, spinning prevails on bending and the top joint undergoes almost only vertical displacements. At the turning point A, a plane of minimum bending stiffness emerges and the mast begins to bend following the arc AB. At B, a second turning point is encountered, which determines a dramatic decrease in stiffness along the arc BC, interpretable as a *snap-back*. This loss of stiffness is due to the formation of a cylindrical hinge between the third and fourth layers. Here, due to the absence of any horizontal stiffening, the bars of the interposed square fall into a common line. This evidently constitutes the Achilles' heel of the reticulated system. Afterwards, the structure transforms into a mechanism no longer able to sustain any applied loads. The upper layers experience an approximately rigid body rotation, CD, which progresses until ultimate failure near E.

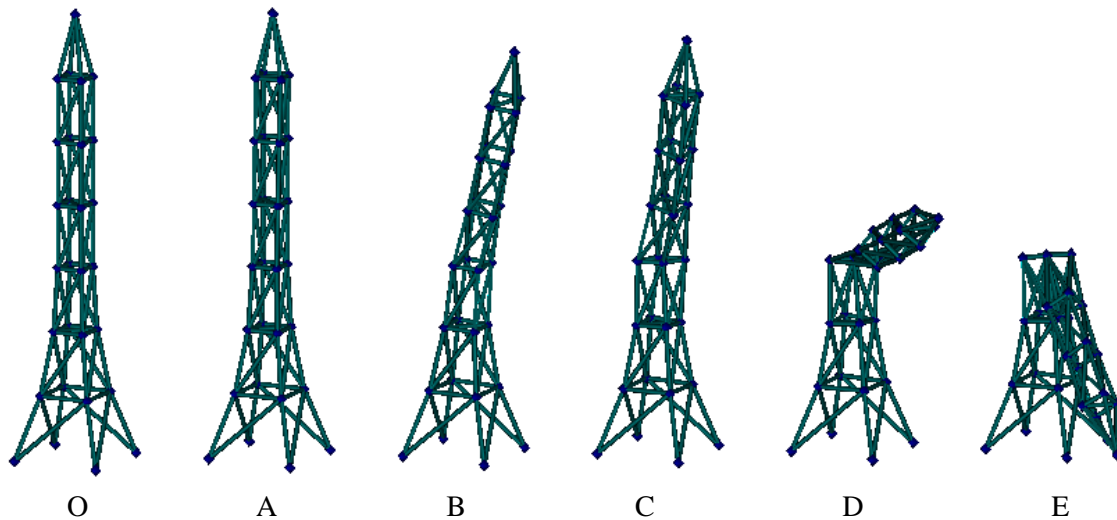


Figure 12: Spirally braced mast with $p_x / p_z = 1/10000$ – Configurations sequence

5.4. A symmetrically braced mast

In analogy to the treatment of the domes, a different bracing scheme is also considered. Here, secondary bars are arranged in such a way as to oppose any possible rotations about the z -axis. The structure possesses two-fold rotational symmetry. As before, a disturbing horizontal load, $P_x = \lambda p_x$, is added to the vertical load, $P_z = \lambda p_z = \lambda \cdot 5000 \text{ daN}$.

Figures 13(a) and 13(b) show two different views of the primary branch relative to the load ratio values, p_x / p_z , indicated in Table 2. The same table also reports the angle, $\bar{\phi}$, and the

limit load multiplier, λ_{\max} . A step-length of $\overline{\Delta\eta} = 2\text{ m}$ was used for the analyses, with $\mu_0 = 1\text{ cm}$ and $TOL = 10^{-6}$.

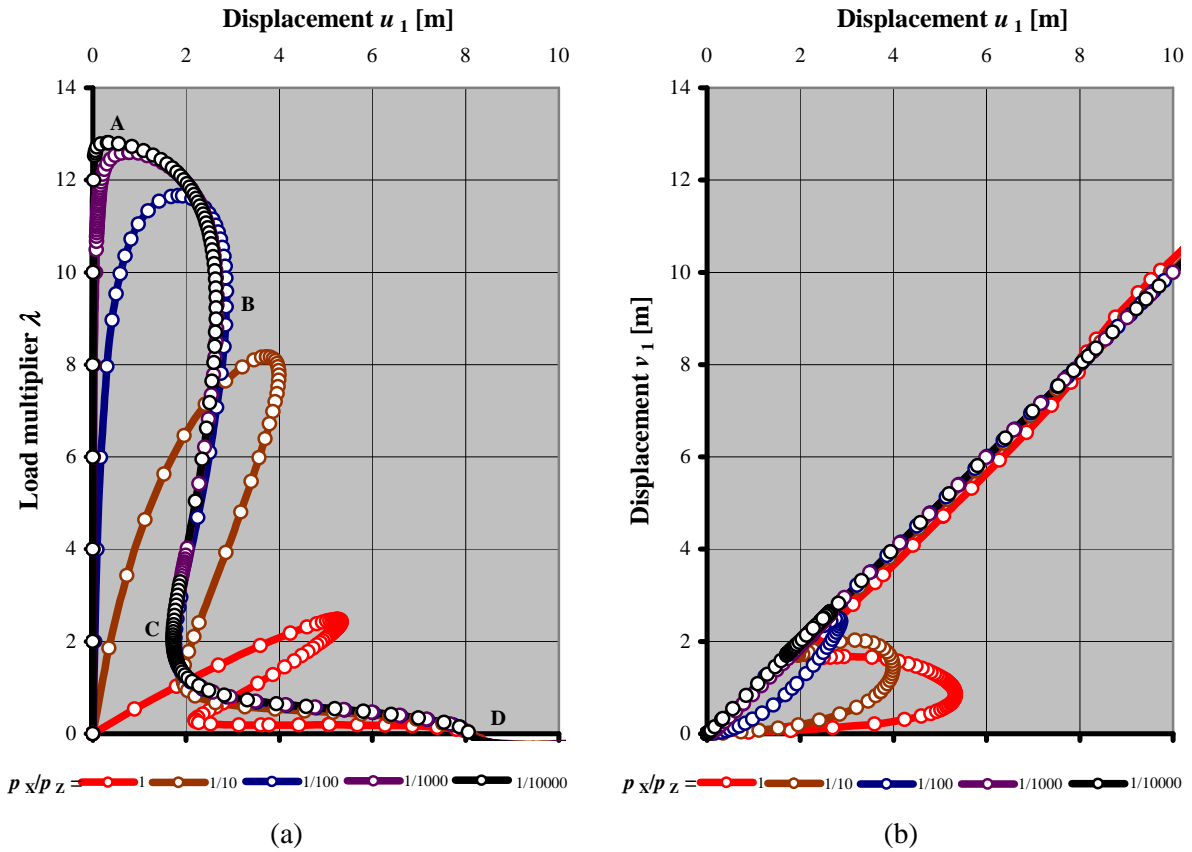


Figure 13: Symmetrically braced mast – Equilibrium path – Joint 1

Figure 14 represents the sequence of configurations along the equilibrium path obtained for the load ratio $p_x / p_z = 1/10000$. Again, the weakest point of the structure is located at the interface between the third and fourth layers, where a cylindrical hinge forms. Regarding the description of the post-critical behaviour, considerations similar to those for the spirally braced case apply.

p_x / p_z	1/1	1/10	1/100	1/1000	1/10000
$\bar{\phi}$	0.025	0.05	0.05	0.025	0.025
λ_{\max}	2.484	8.172	11.661	12.598	12.930

Table 2: Load ratio, half-cone angle and limit loads for the symmetrically braced mast

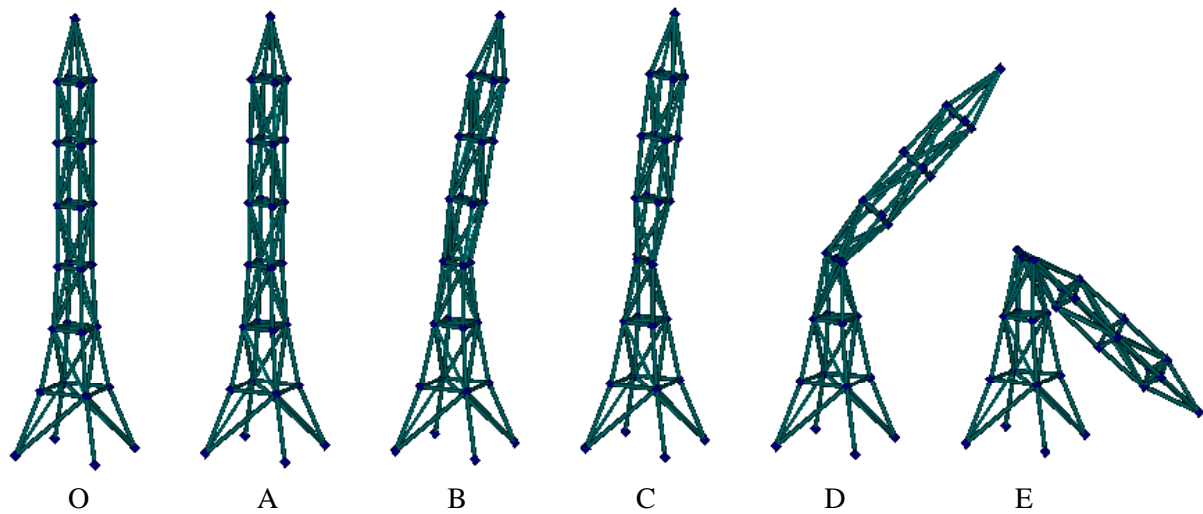


Figure 14: Symmetrically braced mast with $p_x / p_z = 1/10000$ – Configurations sequence

6. Conclusion

A strategy for uniformly accurate tracing of the equilibrium paths of elastic reticulated structures subject to conservative proportional loads was applied to the stability analysis of two classes of Schwedler domes and three-dimensional masts with different bracing schemes. The strategy proves capable of highly accurate tracing of complex tangled equilibrium paths endowed with nearly inextricable knots and sharp turning points.

References

- [1] G.A. Wempner: *Discrete approximation related to nonlinear theories of solids*. Int. J. Solids Structures, **7**, (1971), 1581–1599.
- [2] E. Riks: *An incremental approach to the solution of snapping and buckling problems*. Int. J. Solids Structures, **15**, (1979), 529–551.
- [3] M.A. Crisfield: *A fast incremental/iterative solution procedure that handles snap-through*. Computers & Structures, **13**, (1981), 55–62.
- [4] S. Ligarò and P. Valvo: *A self-adaptive strategy for uniformly accurate tracing of the equilibrium paths of elastic reticulated structures*. Int. J. Num. Methods Eng., in press.
- [5] P. Wriggers, W. Wagner and C. Miehe: *A quadratically convergent procedure for the calculation of stability points in finite element analysis*. Comput. Meths. Appl. Mech. Engrg., **70**, (1988), 329–347.